

Ammonium-Functionalized Naphthalene Diimides as Two-Electron-Transfer Negolyte for Aqueous Redox Flow Batteries

Vikram Singh,^[a, b] Seongmo Ahn,^[a] and Hye Ryung Byon^{*[a]}

Aqueous organic redox flow batteries (AORFBs) have been developed as safe and economical energy storage systems for renewable energy applications. Herein, the solubility of two-electron-transfer organic molecules, naphthalene diimides (NDIs), was improved by adding two propyl-spaced ammonium functionalities. Under neutral conditions, the di-ammonium-functionalized NDIs exhibited a solubility of ~ 0.7 M (1.4 M/e $^-$) in water. Using 0.3 M NDIs as negolyte (negative electrolyte) and

iodide/triiodide as posolyte (positive electrolyte), AORFBs achieved 300 galvanostatic cycles with approximately 100% capacity retention. The post-mortem analyses revealed negligible chemical decomposition with no crossover while using a Nafion membrane. This study presents a promising NDI negolyte that can achieve stable two-electron transfer in AORFBs.

Introduction

The use of renewable and environmentally friendly energy sources for generating electricity has gained significant interest in advanced energy storage applications.^[1] Various energy storage systems (ESSs) are used in conjunction with solar, wind, biomass, and hydropower systems to provide a stable electric supply.^[2] When designing an ESS, safety, low cost, and low maintenance should be considered. Accordingly, various aqueous batteries, including redox flow batteries (RFBs), have been developed. The advantages of RFBs include their flexible cell configurations owing to liquid-phase active materials and the ability to decouple power and energy outputs.^[3] Vanadium-based RFBs are among the most widely used ESSs. However, it is necessary to develop new redox-active materials for RFBs, owing to the rising costs of vanadium.^[4]

Recently, organic redox-active molecules have been intensively studied and applied to develop aqueous organic RFBs (AORFBs).^[3a,5] The molecular designing of organic redox-active materials enables the tuning of solubility, redox potential, and chemical stability. Additionally, multi-electron transfer increases the total energy density by multiple times. Viologens and anthraquinones are redox molecules that undergo a two-electron ($2e^-$) transfer.^[6] Under different pH conditions and with various functional groups, such as sulfonate,^[6c]

phosphonate,^[7] ammonium,^[6d,8] and carboxylate,^[6f,9] their chemical/ electrochemical stability and solubility were investigated. Importantly, undesired chemical reactions were mitigated at neutral pH. In addition, the volumetric energy density of the AORFBs was enhanced without the addition of proton and hydroxide ions.^[1c,10] However, anthraquinone undergoes proton-coupled electron transfer in neutral media, leading to a significant pH increase during galvanostatic charging and discharging processes.^[11] The instability and dimerization of fully reduced viologen limits the second electron transfer process.^[12] Delicate synthetic procedures are required to stabilize viologen reactions.^[6d,12,13] Therefore, it is necessary to explore new candidates for the $2e^-$ transfer of organic molecules.

We investigated naphthalene diimides (NDIs) as chemically stable and $2e^-$ transferred negolytes. Methyl NDI (Me-NDI) is immiscible at neutral pH in aqueous medium because of the strong π - π stacking interactions between NDI cores.^[14] Thus, chemical substitutes are needed to improve the solubility, and only a few studies were attempted either using *N*-alkylation or NDI core substitution.^[15] Previously, we also developed carboxylated-functionalized NDI (K₂-BNDI).^[9a] However, the obtained solubility of ~ 0.2 M (≈ 0.4 M/e $^-$) in a neutral aqueous electrolyte solution did not meet the prerequisites of RFBs. Herein, we designed di-ammonium functionalized NDIs and increased the solubility of the material up to ~ 0.7 M (≈ 1.4 M/e $^-$) in water and ~ 0.5 M (≈ 1.0 M/e $^-$) in 1.5 M KCl (aq.). Coupled with NH₄I as the posolyte, AORFBs with 0.3 M of NDI (≈ 0.6 M/e $^-$) showed stable $2e^-$ transfer and negligible capacity decay over 300 cycles. These results demonstrate the potential of highly stable NDI negolytes as future organic redox-active materials.

[a] Dr. V. Singh, S. Ahn, Prof. H. R. Byon
Department of Chemistry
Korea Advanced Institute of Science and Technology (KAIST)
Advanced Battery Center, KAIST Institute for NanoCentury
291 Daehak-ro, Yuseong-gu, Daejeon 34141, Republic of Korea
E-mail: hrbyon@kaist.ac.kr

[b] Dr. V. Singh
Natural Science Research Institute, KAIST
291 Daehak-ro, Yuseong-gu, Daejeon 34141, Republic of Korea

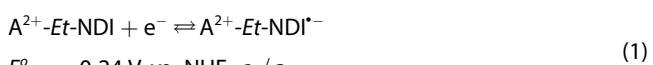
 Supporting information for this article is available on the WWW under
<https://doi.org/10.1002/batt.202200281>

 An invited contribution to a Special Collection on Organic Batteries

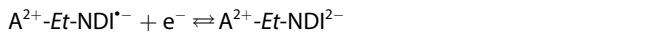
Results and Discussion

A di-ammonium-functionalized NDI, denoted as $\text{A}^{2+}\text{-Et-NDI}$, was synthesized through the *N*-alkylation of 1,4,5,8-naphthalene tetracarboxylic dianhydride (NTCDA), followed by substitution with 1-bromoethane (Figures 1a, S1 and S2). The resulting $\text{A}^{2+}\text{-Et-NDI}\cdot\text{2Br}^-$ powder had a pale yellow color and was of high purity. In addition, the prepared $\text{A}^{2+}\text{-Et-NDI}$ powders were thermally stable, showing a negligible change in ^1H NMR spectra after immersing the powder in D_2O for seven days at both room temperature and 70°C (Figure 1b). The maximum solubility of $\text{A}^{2+}\text{-Et-NDI}$ was 0.7 M in water and 0.5 M in 1.5 M KCl (aq.) (Figures 1c and S3). A significant increase in solubility compared to that of previously reported methyl NDI and carboxylated NDI^[9a] resulted from the highly soluble di-ammonium groups in neutral aqueous media.

Cyclic voltammetry (CV) analysis shows two redox waves at formal potentials of -0.24 (c_1/a_1) and -0.54 V (c_2/a_2) vs. Normal Hydrogen Electrode (NHE) in 1.0 M KCl solution (Figures 1d and S4), where c and a refers to the cathodic and anodic signals, respectively. These redox waves, denoting $\text{NDI}^{\bullet-}$ and NDI^{2-} formation [Equations (1) and (2)], were stable over 500 cycles at a scan rate of 50 mV s^{-1} (Figure S5).



$$E_1^\circ = -0.24 \text{ V vs. NHE, } c_1/a_1$$



$$E_2^\circ = -0.54 \text{ V vs. NHE, } c_2/a_2$$

The c_1 wave was broader than c_2 , and the peak-to-peak potential (ΔE) for c_1/a_1 (120 mV) was wider than that for c_2/a_2 (60 mV). This indicates slower charge-transfer kinetics for the first redox event than for the subsequent event. This observation was also supported by the estimated electron-transfer rate

(k^o , Figure S6), which showed that c_1/a_1 ($3.12 \times 10^{-2} \text{ cm s}^{-1}$) was one order of magnitude lower than the c_2/a_2 ($1.71 \times 10^{-1} \text{ cm s}^{-1}$). In comparison, the diffusion coefficients (D) of $\text{A}^{2+}\text{-Et-NDI}^{\bullet-}$ and $\text{A}^{2+}\text{-Et-NDI}^{2-}$ were similar with values of $2\text{--}3 \times 10^{-6} \text{ cm}^2 \text{ s}^{-1}$ (Figure S7). Moreover, the $\text{A}^{2+}\text{-Et-NDI}$ redox reactions did not interfere with different electrolyte salts, such as Na^+ , K^+ , NH_4^+ , Cl^- , Br^- , and NO_3^- (Figure S8).

Next, static H-cells were used to examine the chemical/electrochemical stability of $\text{A}^{2+}\text{-Et-NDI}$ under galvanostatic conditions. Symmetric and static H cells were composed of 6 mL of 5 mM as-prepared $\text{A}^{2+}\text{-Et-NDI}$ as negolyte and 6 mL of $\text{A}^{2+}\text{-Et-NDI}^{2-}$ (i.e., 100% state of charge (SOC) of $\text{A}^{2+}\text{-Et-NDI}$) as posolyte. 1 M KCl was added as a supporting electrolyte on both sides, and a Nafion 212 membrane with a thickness of 50 μm was installed between the two containers (Figure 2a). Stable galvanostatic cycling was observed over 100 cycles (Figure 2b). There was only a marginal capacity decay during the first few cycles, but the overall capacity was retained at $\sim 0.2 \text{ mAh}$ for 100 cycles, demonstrating the chemical and electrochemical stability of $\text{A}^{2+}\text{-Et-NDI}$. Additionally, two potential plateaus at approximately -0.24 and -0.54 V vs. NHE were observed and were consistent with the above formal potentials in the CV.

A cation exchange membrane (Nafion 212) was used with $\text{A}^{2+}\text{-Et-NDI}$ for both static and full AORFBs because the posolyte using iodide/triiodide (I^-/I_3^-) easily undergoes crossover (see below). Therefore, the negolyte design should also consider crossover, which was reduced even with a cation-exchange membrane. We expected that the propyl spacers and ammonium groups would increase the NDI molecular size and mitigate the crossover of $\text{A}^{2+}\text{-Et-NDI}$ through size exclusion. Permeability tests were conducted using the H-cell containing 6 mL of 0.1 M $\text{A}^{2+}\text{-Et-NDI}$ in 1.0 M KCl (aq.) on one side and 6 mL of 1.2 M KCl on the other side (Figure S9). The ionic strengths on both sides were balanced to avoid osmotic

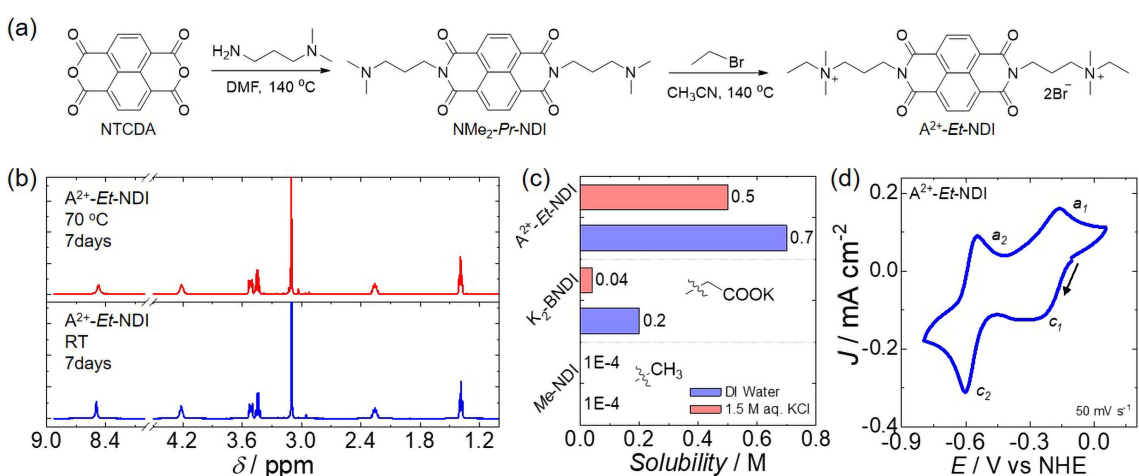


Figure 1. Characterizations of $\text{A}^{2+}\text{-Et-NDI}$. a) Two-step synthetic protocols for $\text{A}^{2+}\text{-Et-NDI}$. b) ^1H NMR spectra of $\text{A}^{2+}\text{-Et-NDI}$ at 70°C (top) and room temperature (bottom) after 7 days storage. c) Comparative solubilities of functionalized NDIs, $\text{A}^{2+}\text{-Et-NDI}$, 2 K^+ -carboxylated-NDI ($\text{K}_2\text{-BNDI}$), and methyl NDI (Me-NDI) (from top to bottom) in water (violet) and in 1.5 M KCl (aq.) (light red). All solubilities were measured using UV-vis spectral analysis. d) Cyclic voltammogram (CV) of 1 mM $\text{A}^{2+}\text{-Et-NDI}$ in 1.0 M KCl (aq.) at a scan rate of 50 mV s^{-1} . The working, counter, and references electrodes were glassy carbon, Pt wire, and Ag/AgCl, respectively.

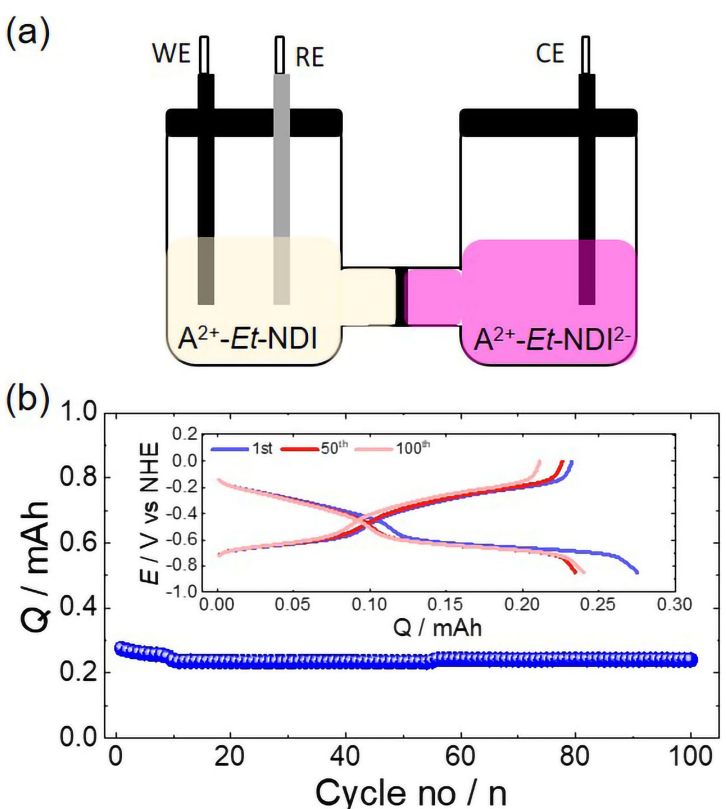


Figure 2. Stability test using a static and symmetric H-cell. a) Schematic view with 6 mL of 5 mM A^{2+} -Et-NDI as negolyte and 6 mL of A^{2+} -Et-NDI $^{2-}$ (100% SOC of A^{2+} -Et-NDI) as posolyte in 1 M KCl. WE, CE and RE: working, counter, and reference electrodes. (b) Galvanostatic cycling test for 100 cycles at a current density of 100 mA g $^{-1}$. The inset shows the corresponding charge-discharge profile.

pressure. The UV-vis spectral method was used to measure the increased concentration of A^{2+} -Et-NDI ($\pi \rightarrow \pi^*$ transition at $\lambda_{\text{max}} = 361$ nm)^[16] in an NDI-free container over time. The permeability of A^{2+} -Et-NDI was $\sim 2.19 \times 10^{-12}$ cm 2 s $^{-1}$, which was reasonably small and comparable to that of viologen derivatives at neutral pH.^[7b]

The negolyte of 50 mM A^{2+} -Et-NDI and the posolyte of 0.2 M NH $_4$ I [I^-/I_3^- , Equation (3)] were then assembled with a 1.0 M KCl solution (Figure 3a and b) for complete AORFB tests. The concentration of NH $_4$ I was 3.1 times higher than that of the negolyte.



Carbon nanotube-loaded carbon felt (area: 6 cm 2) was used as an electrode on both sides. A K $^+$ -exchanged Nafion 212 membrane exhibited an area-specific resistance (ASR) of 0.6 Ω cm 2 under the given condition (Figure S10).

Galvanostatic profiles displayed two charging and discharging plateaus, corresponding to the difference in redox potentials from negolyte and posolyte at 0.84 V and 1.17 V, respectively (Figure 3c). Upon applying a current density of 10 mA cm $^{-2}$ and a flow rate of 40 mL min $^{-1}$, the transparent negolyte solution turned maroon at 50% SOC (Figure 3d). Correspondingly, the $\pi \rightarrow \pi^*$ transition band of NDI centered at 361 nm disappeared, whereas a new band appeared at 449 nm in the visible region, which was associated with the formation

of NDI $^{*+}$ (Figure 3e). At 100% SOC, the negolyte solution turned pink (Figure 3d). In addition, multiple visible bands were observed at 405, 526, and 571 nm, which were assigned to ND I^{2-} , while the NDI $^{*+}$ band disappeared (Figure 3e). In the near-IR region, an intense absorption band appeared in the 800–1500 nm region at 50% SOC but not at 0% and 100% SOC (Figure S11). This may be attributed to the enhanced π - π stacking of NDI $^{*+}$ molecules through spin-pairing interactions.^[17] Presumably, A^{2+} -Et-NDI $^{*+}$ molecules formed a short-range order stacking, forming a cluster instead of a large precipitate because neither any precipitation nor any capacity decrease was observed. The cluster might have been disassembled in the following cathodic reaction forming A^{2+} -Et-NDI $^{2-}$ because of the disappearance of the spin-pairing interaction, while only the strong Coulombic repulsion among ND I^{2-} remains. 1 H NMR spectroscopic analyses revealed an intramolecular interaction between the positively charged ammonium groups and the negatively charged NDI core. At 100% SOC, hydrogen signals associated with both ammonium and terminal methyl groups significantly shifted upfield (Figure 3f). This implied that the ammonium moiety was in close proximity to the NDI $^{2-}$ core and triggered intramolecular interactions. Accordingly, the intermolecular interactions between the ammonium moiety and the Br $^-$ counterion became weak. Unlike the previously reported study on carboxylated-NDI, in which the carboxylate group was intimately paired with the K $^+$ counterion, the present study provided distinct

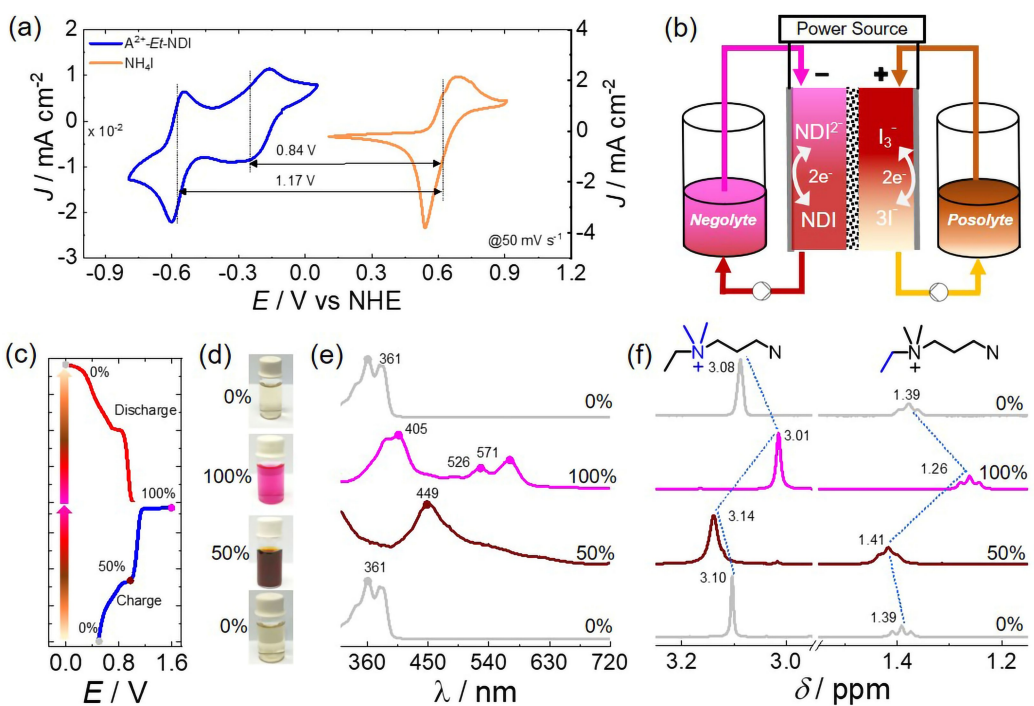


Figure 3. Characterizations of A^{2+} -Et-NDI in AORFBs. a) CV curves of A^{2+} -Et-NDI and $\text{I}^-|\text{I}_3^-$ on glassy carbon as the working electrode at a scan rate of 50 mV s^{-1} . b) Schematic illustration of AORFB configuration. A^{2+} -Et-NDI and NH_4^+ were negolyte and posolyte, respectively, and Nafion 212 was used as the membrane. c) A typical charge-discharge curve with $50 \text{ mM } \text{A}^{2+}$ -Et-NDI (10 mL) || $0.2 \text{ M } \text{NH}_4^+$ (20 mL) and 1.0 M KCl electrolyte. The flow rate was 40 mL min^{-1} . The arrows indicate color changes that accompanied the redox process during a charge and a discharge event. d) UV-vis absorption spectra and e) ^1H NMR spectra of $50 \text{ mM } \text{A}^{2+}$ -Et-NDI with respect to 0, 50, and 100% SOC.

results.^[9a] This ion pairing likely induced gradual integration between the first and second reduction plateaus,^[9a] which was not observed in A^{2+} -Et-NDI.

After the complete discharging process, the UV-vis spectra and ^1H NMR chemical shifts returned to the initial state. This demonstrates the reversibility of A^{2+} -Et-NDI redox processes. In addition, the electrochemical oxidation processes in the UV-vis spectra were similar to the chemical oxidation of A^{2+} -Et-NDI $^{2-}$ in air, as shown by the time-dependent transitions (Figure S12), demonstrating the insignificant electrochemical decomposition of A^{2+} -Et-NDI. In addition, ^1H NMR spectra verified the chemical stability of A^{2+} -Et-NDI $^\bullet-$ and A^{2+} -Et-NDI $^{2-}$, showing no thermal degradations at 70°C for 7 days (Figures S13 and S14).

For the performance tests, 0.3 M of A^{2+} -Et-NDI (10 mL) was assembled with $1.0 \text{ M } \text{NH}_4^+$ (20 mL) in AORFBs using 1.0 M KCl as electrolyte. The pH of the negolyte and the posolyte solution was ~ 7.2 and ~ 6.0 , respectively. Galvanostatic curves at the second cycle were compared at current densities of $5, 10, 15, 20, 25$, and 30 mA cm^{-2} and a fixed flow rate of 40 mL min^{-1} , as shown in Figure 4(a). The AORFBs utilizing 0.3 M ($\approx 0.6 \text{ M/e}^-$) of A^{2+} -Et-NDI delivered a capacity of 13.42 Ah L^{-1} at 5 mA cm^{-2} , which was 83.45% of the theoretical capacity. In addition, the voltage and energy efficiencies were estimated to be 79% and 76% at 5 mA cm^{-2} and 71% and 69% at 10 mA cm^{-2} , respectively. When the current density was increased from 10 to 30 mA cm^{-2} , the Coulombic efficiency (CE) also increased from 96.18% to 99.05% (Figure 4b). The polarization curves at

100% SOC revealed a maximum power density of $\sim 28 \text{ mW cm}^{-2}$ (Figure S15).

Notably, the first charging event (c_1) was significantly shorter than the second charging plateau (c_2), and these behaviors diminished the total capacities, in particular for higher current densities (Figure 4a and c). The first galvanostatic curve designated the origin of this behavior as a short A^{2+} -Et-NDI $^\bullet-$ oxidation process (the second discharging event, a_1), which shortened the following first charging curve (c_1) in the second cycle (Figure 4d). Because this capacity reduction could be related to the cell polarization resistance,^[18] we held a constant voltage at 1.7 V and 0.0 V after the galvanostatic charging and discharging process, respectively. This constant-voltage mode did not shrink the first charging plateau during the 2nd cycle and even extended the second discharging plateau at the 80th cycle (Figure 4e). A total discharging capacity approached $\sim 99.36\%$ of the theoretical one at the 80th cycle, which was higher than the pure galvanostatic one (without the constant-voltage mode) at $\sim 55.12\%$. All these examinations confirmed stable A^{2+} -Et-NDI. In addition, the small second discharging plateau in the galvanostatic mode is presumed due to the clustering of A^{2+} -Et-NDI $^\bullet-$, thus slowing mass transport.

The AORFBs showed excellent stability for galvanostatic 300 cycles at 30 mA cm^{-2} . The stable charge-discharge profiles appeared at the 2nd, 100th, 200th and 300th cycles (Figure 4c). The capacity fading rate was 0.0026% per cycle and 0.075% per day estimated in 100–185 cycles, while there was no

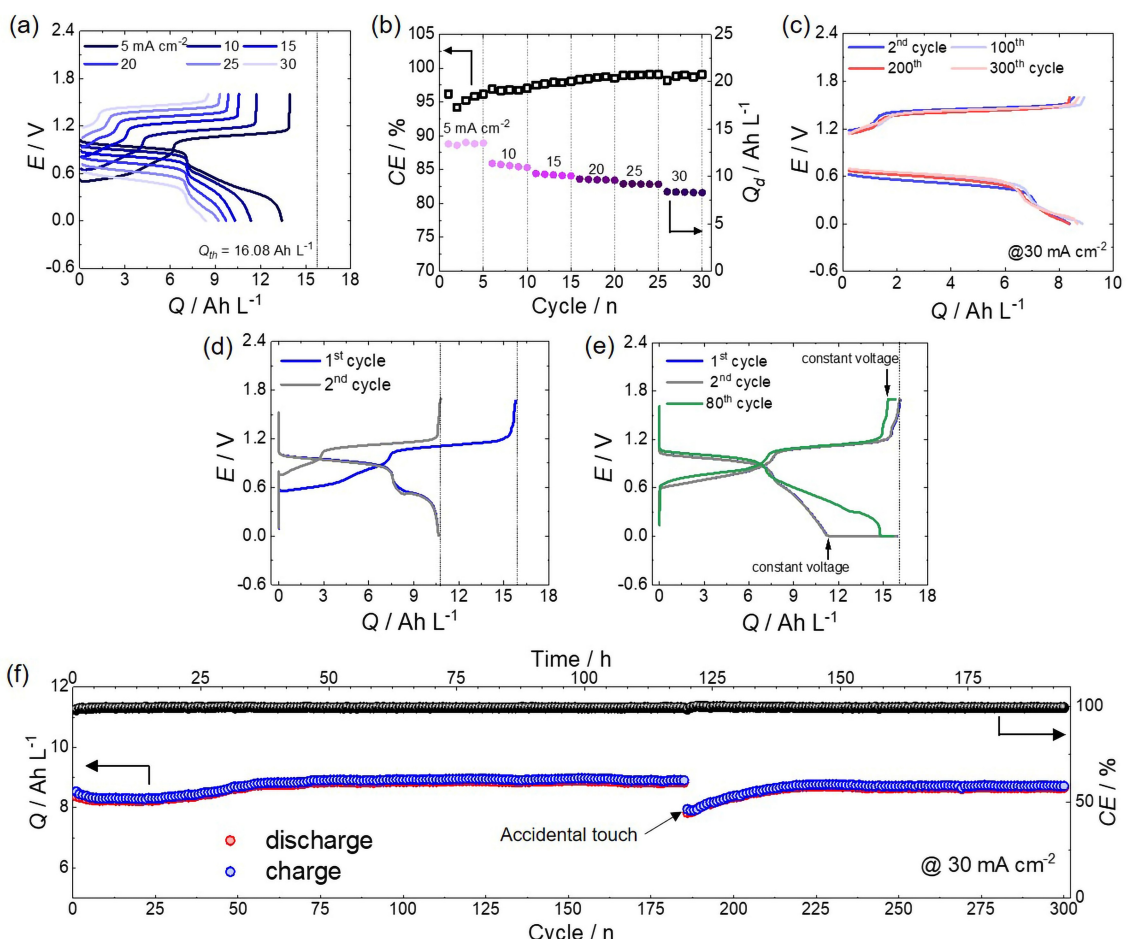


Figure 4. Galvanostatic investigation of 0.3 M of A^{2+} -Et-NDI (10 mL) || 1.0 M of NH_4I (20 mL) in AORFBs. The flow rate was 40 mL min^{-1} . a) Second charge-discharge profile at a current density of 5, 10, 15, 20, 25, and 30 mA cm^{-2} . The theoretical capacity at 0.3 M of A^{2+} -Et-NDI is 16.08 Ah L^{-1} . b) Rate-capability test conducted for five cycles with increasing current densities. CE represents coulombic efficiency. c) Representative charge-discharge profile for the 2nd, 100th, 200th and 300th cycles at 30 mA cm^{-2} . d) Galvanostatic profiles for the 1st and 2nd cycle at a current density of 30 mA cm^{-2} . e) The constant-voltage mode graphs at 1.7 V after the galvanostatic charge and 0.0 V after the galvanostatic discharge at a current density of 30 mA cm^{-2} until the current density approached below 2 mA cm^{-2} . f) Galvanostatic cycling performance for 300 cycles. The abrupt capacity drop at the 186th cycle was due to accidental touching of the connecting wire.

capacity loss during 250–300 cycles (Figure 4f). We note that abrupt capacity fading at the 186th cycle was due to accidental touching of the connecting wire of AORFBs, but the capacity was recovered. After 300 cycles, the cell maintained an average CE of 99.34%. All these results were superior to a previous study using 0.5 M N,N'-bis(dimethylaminopropyl)-NDI coupled with 1,1'-bis[3-(trimethylammonio)propyl]ferrocene dichloride, showing a capacity fading rate of ~0.26% per cycle for a total 60 cycle.^[15c] The difference was due to side reactions from the crossover ferrocene posolyte.^[15c]

We extracted both the negolyte- and posolyte-side solutions to investigate crossover and chemical decomposition. There was no A^{2+} -Et-NDI signal in the CV from the posolyte-side solution after 300 cycles (Figure S16), verifying no negolyte crossover. However, notable I^-/I_3^- redox signals appeared from the negolyte-side solution, demonstrating a significant posolyte crossover through the cation-exchange membrane. Indeed, the permeability of I^-/I_3^- ($6.71 \times 10^{-11} \text{ cm}^2 \text{s}^{-1}$ from the mixture of 0.01 M I_2 and 0.2 M NH_4I) was ~30 times higher than that of A^{2+} -

-Et-NDI ($\sim 2.19 \times 10^{-12} \text{ cm}^2 \text{s}^{-1}$) (Figure S17). This result is not related to the membrane fouling by the inserted and clogged A^{2+} -Et-NDI,^[19] because the test was done in the absence of a negolyte, but may be associated with I^-/I_3^- interaction with Nafion. Further study is needed in the near future. Nonetheless, the I^-/I_3^- crossover did not cause side reactions; ¹H NMR spectra of the negolyte-side electrolyte solutions after 300 cycles revealed a minute A^{2+} -Et-NDI decomposition (Figures S18 and S19). In addition, stable redox waveforms were observed in the CV analysis, even from the mixture of A^{2+} -Et-NDI and NH_4I , suggesting the absence of chemical interference from the two redox couples during the entire electrochemical process (Figure S20). It was worth noting that insertion and clogging of A^{2+} -Et-NDI into Nafion 212 membrane occurred to some degree. A moderate increase in membrane resistance was observed after galvanostatic intermittent titration (GITT) tests in symmetric A^{2+} -Et-NDI cells (Figure S21). However, this resistance was smaller than other redox species, such as 1,1'-bis[3-(trimethylammonio)propyl] ferrocene dichloride and methyl

vionogen.^[19] The insignificant capacity loss over 300 cycles and no crossover of A²⁺-Et-NDI also demonstrated that the di-ammonium substituents did not critically interfere with the membrane.

Conclusion

The solubility of NDI molecules was increased by attaching di-ammonium functionality to achieve a maximum solubility of 0.7 M (\approx 1.4 M/e⁻) in water. The resulting di-ammonium NDI also showed stable 2e⁻ transfer processes as evident from UV-vis spectra and ¹H NMR analyses at distinct SOCs in AORFBs. A 0.3 M solution of di-ammonium NDI (\approx 0.6 M/e⁻) achieved 300 cycles with approximately 100% capacity retention in AORFBs upon pairing with iodide/triiodide posolyte. Despite using the cation-exchange membrane, there was no evidence of crossover for di-ammonium NDI molecules, possibly because of the enlarged NDI size owing to the propyl spacers and ammonium groups. In addition, their inability to interfere with iodide/triiodide over 300 cycles demonstrated their excellent chemical stability. Compared to our previous study using carboxylated-NDI pairing with a K⁺ counterion,^[9a] the ammonium functionality introduction to NDI achieved higher solubility. The ion pairing between ammonium and the Br⁻ counterion was insignificant. Instead, the clustering of A²⁺-Et-NDI⁻ and the intramolecular interaction between ammonium and NDI²⁻ were more pronounced. This study highlighted the importance of molecular interactions in understanding molecular solubility and electrochemical behaviors, which would further guide the improvements in molecular solubility and stability in future designs.

Experimental Section

Synthesis of A²⁺-Et-NDI (3,3'-(1,3,6,8-tetraoxo-1,3,6,8-tetrahydrobenzo[1,2*n*][3,8]phenanthroline-2,7-diyl)bis(*N*-ethyl-*N,N*-dimethylpropan-1-aminium):

Step 1. Synthesis of NMe₂-Pr-NDI (2,7-bis(3-(dimethylamino)propyl)benzo[1,2*n*][3,8]phenanthroline-1,3,6,8(2*H*,7*H*)-tetraone). 3.0 g of 1,4,5,8-Naphthalenetetracarboxylic dianhydride (NTCDA) was added to 20 mL of anhydrous DMF in a 100 mL round bottom flask with stirring and argon atmosphere. 3-(Dimethylamino)-1-propylamine (5 equiv.) was added to the mixture dropwise with vigorous stirring. The solution turned green and viscous and refluxed at 150°C overnight. The reaction was cooled down to room temperature without stirring, resulting in green needle-shaped crystals of NMe₂-Pr-NDI. The crystals were collected by simple filtration and washed with DMF, acetone, and diethyl ether. The yield of NMe₂-Pr-NDI: 4.0 g (92%). ¹H NMR (CDCl₃, 300 MHz): δ 8.78 (s, 4H, Ar-H), δ 4.29 (t, 4H, -N_{imide}-CH₂-), δ 2.45 (t, 4H, -N_{imide}-CH₂-), δ 2.25 (s, 12H, -N(CH₃)₂), δ 1.94 (quint, 4H, -CH₂-CH₂-CH₂).

Step 2. A 250 mL round bottom flask was charged with 4.0 g of NMe₂-Pr-NDI and 100 mL of acetonitrile. An excess of 1-bromoethane (5 equiv.) was added, and the mixture was refluxed at 140°C for 16 h. The solution became clear at 100–110°C and then gradually resulted in an off-white precipitate. The precipitate was filtered after cooling to room temperature and washed with

acetonitrile, chloroform, and acetone. After drying under vacuum, the precipitate was dissolved in a minimum amount of water and reprecipitated with acetone. This dissolution and reprecipitation were repeated three times. During this time, the off-white precipitate turned to light yellow to yellow color. Finally, the precipitate was dried at 100°C under a vacuum. Yield→A²⁺-Et-NDI=4.0 g (85%). ¹H NMR (D₂O, 400 MHz) of A²⁺-Et-NDI: δ 8.51 (s, 4H, Ar-H), δ 4.21 (t, 4H, -N_{imide}-CH₂-), δ 3.54–3.49 (m, 4H, -CH₂-N⁺(CH₃)₂(C₂H₅)), δ 3.43 (q, 4H, -N⁺(CH₃)₂(CH₂CH₃)), δ 3.10 (s, 12H, -CH₂-N⁺(CH₃)₂(C₂H₅), δ 2.32–2.21 (m, 4H, -CH₂-CH₂-CH₂), δ 1.39 (t, 6H, -CH₂-CH₃). ¹H and ¹³C NMR spectra were recorded at Bruker AVNEO 400 MHz spectrometer. Chemical shifts were expressed in ppm values with residual solvent resonance as the internal standard (D₂O, δ=4.79; CDCl₃, δ=7.26). All spectra were recorded at 298 K.

Construction of a redox flow cell: A zero-gap flow cell was assembled with two carbon felt electrodes coated with carbon nanotubes (97%, diameter= ~20 nm, length= ~10 μm; ACN Tech. Co. Ltd.) and sandwiched with Nafion 212 K⁺ exchange membrane (thickness=50.8 μm). The active area of the flow cell was 6 cm² determined by the geometrical area of the carbon electrode. The negolyte reservoir contained 10 mL of the negolyte solution (A²⁺-Et-NDI) in 1.5 M KCl(aq). The posolyte reservoir contains 20 mL of NH₄I in 1.5 M KCl(aq), where the concentration of NH₄I was 3.1 times higher than the corresponding negolyte one. Both reservoirs were purged with Ar gas for 30 min and sealed. Peristaltic pumps for flowing the redox-active materials were purchased from Shencheng, model LabV1 and/or from Masterflex model 77202-60. Norprene Tubing (O.D.=16) from Masterflex was used to flow the liquids. The solutions were circulated through the flow cell at a flow rate of 40 mL min⁻¹. The flow cells were galvanostatically cycled at room temperature within the voltage window of 0.0 to 1.7 V at current densities ranging from 5–30 mA cm⁻². The volumetric capacity was calculated by taking the volume of the negolyte alone. The theoretical capacity (Q_t) was estimated using Equation (4).

$$\text{Capacity (Q}_t\text{)} = mnF/MV \quad (4)$$

where *m* is the mass of the active material (g), *n* is the number of electrons, *F* is the Faraday's constant (26.8 Ah), *M* is the molar mass of the active material (g mol⁻¹), and *V* is the volume of the posolyte or negolyte (L).

Acknowledgements

This work was supported by the Samsung Research Funding & Incubation Center of Samsung Electronics under Project Number SRFC-MA1702-05. VS thanks Basic Science Research Program through the National Research Foundation of Korea (NRF) funded by the Ministry of Education (2019R1A6A1A10073887).

Conflict of Interest

The authors declare no conflict of interest.

Data Availability Statement

The data that support the findings of this study are available in the supplementary material of this article.

Keywords: iodide · naphthalene diimides · organic redox molecules · redox flow batteries · two electron-transfer

- [1] a) B. Dunn, H. Kamath, J.-M. Tarascon, *Science* **2011**, *334*, 928–935; b) J. Rugolo, M. J. Aziz, *Energy Environ. Sci.* **2012**, *5*, 7151–7160; c) D. G. Kwabi, Y. Ji, M. J. Aziz, *Chem. Rev.* **2020**, *120*, 6467–6489.
- [2] a) Z. Yang, J. Zhang, M. C. Kintner-Meyer, X. Lu, D. Choi, J. P. Lemmon, J. Liu, *Chem. Rev.* **2011**, *111*, 3577–3613; b) P. T. Moseley, J. Garche, *Electrochemical energy storage for renewable sources and grid balancing*, Elsevier **2014**.
- [3] a) V. Singh, S. Kim, J. Kang, H. R. Byon, *Nano Res.* **2019**, *12*, 1988–2001; b) Z. Li, Y. C. Lu, *Adv. Mater.* **2020**, *32*, 2002132; c) P. Leung, A. Shah, L. Sanz, C. Flox, J. Morante, Q. Xu, M. Mohamed, C. P. De León, F. Walsh, *J. Power Sources* **2017**, *360*, 243–283; d) K. Lourenssen, J. Williams, F. Ahmadpour, R. Clemmer, S. Tasnim, *J. Energy Storage* **2019**, *25*, 100844.
- [4] a) M. Wu, M. Bahari, Y. Jing, K. Amini, E. M. Fell, T. Y. George, R. G. Gordon, M. J. Aziz, *Batteries & Supercaps* **2021**, *5*, e202200009; b) Z. Huang, A. Mu, L. Wu, B. Yang, Y. Qian, J. Wang, *ACS Sustainable Chem. Eng.* **2022**, *10*, 7786–7810; c) J. H. Vinco, A. E. E. da Cunha Domingos, D. C. R. Espinosa, J. A. S. Tenório, M. d P. G Baltazar, *J. Energy Storage* **2021**, *43*, 103180.
- [5] a) Q. Chen, Y. Lv, Z. Yuan, X. Li, G. Yu, Z. Yang, T. Xu, *Adv. Funct. Mater.* **2022**, *32*, 2108777; b) R. Feng, X. Zhang, V. Murugesan, A. Hollas, Y. Chen, Y. Shao, E. Walter, N. P. Wellala, L. Yan, K. M. Rosso, *Science* **2021**, *372*, 836–840; c) B. Hu, M. Hu, J. Luo, T. L. Liu, *Adv. Energy Mater.* **2022**, *12*, 2102577; d) X. Li, P. Gao, Y.-Y. Lai, J. D. Bazak, A. Hollas, H.-Y. Lin, V. Murugesan, S. Zhang, C.-F. Cheng, W.-Y. Tung, *Nat. Energy* **2021**, *6*, 873–881; e) M. R. Gerhardt, L. Tong, R. Gómez-Bombarelli, Q. Chen, M. P. Marshak, C. J. Galvin, A. Aspuru-Guzik, R. G. Gordon, M. J. Aziz, *Adv. Energy Mater.* **2017**, *7*, 1601488.
- [6] a) B. Huskinson, M. P. Marshak, C. Suh, S. Er, M. R. Gerhardt, C. J. Galvin, X. Chen, A. Aspuru-Guzik, R. G. Gordon, M. J. Aziz, *Nature* **2014**, *505*, 195–198; b) T. Janoschka, N. Martin, U. Martin, C. Fribe, S. Morgenstern, H. Hiller, M. D. Hager, U. S. Schubert, *Nature* **2015**, *527*, 78–81; c) C. DeBruler, B. Hu, J. Moss, J. Luo, T. L. Liu, *ACS Energy Lett.* **2018**, *3*, 663–668; d) J. Luo, B. Hu, C. Debruler, T. L. Liu, *Angew. Chem. Int. Ed.* **2018**, *57*, 231–235; *Angew. Chem.* **2018**, *130*, 237–241; e) W. Wu, J. Luo, F. Wang, B. Yuan, T. L. Liu, *ACS Energy Lett.* **2021**, *6*, 2891–2897; f) C. Wang, B. Yu, Y. Liu, H. Wang, Z. Zhang, C. Xie, X. Li, H. Zhang, Z. Jin, *Energy Storage Mater.* **2021**, *36*, 417–426.
- [7] a) Y. Ji, M. A. Goulet, D. A. Pollack, D. G. Kwabi, S. Jin, D. De Porcellinis, E. F. Kerr, R. G. Gordon, M. J. Aziz, *Adv. Energy Mater.* **2019**, *9*, 1900039; b) S. Jin, E. M. Fell, L. Vina-Lopez, Y. Jing, P. W. Michalak, R. G. Gordon, M. J. Aziz, *Adv. Energy Mater.* **2020**, *10*, 2000100.
- [8] B. Hu, J. Luo, M. Hu, B. Yuan, T. L. Liu, *Angew. Chem.* **2019**, *131*, 16782–16789; *Angew. Chem. Int. Ed.* **2019**, *58*, 16629–16636.
- [9] a) V. Medabalmi, M. Sundararajan, V. Singh, M.-H. Baik, H. R. Byon, *J. Mater. Chem. A* **2020**, *8*, 11218–11223; b) A. Hollas, X. Wei, V. Murugesan, Z. Nie, B. Li, D. Reed, J. Liu, V. Sprenkle, W. Wang, *Nat. Energy* **2018**, *3*, 508–514.
- [10] a) Y. Yao, J. Lei, Y. Shi, F. Ai, Y.-C. Lu, *Nat. Energy* **2021**, *6*, 582–588; b) S. Jin, Y. Jing, D. G. Kwabi, Y. Ji, L. Tong, D. De Porcellinis, M.-A. Goulet, D. A. Pollack, R. G. Gordon, M. J. Aziz, *ACS Energy Lett.* **2019**, *4*, 1342–1348.
- [11] L. Xia, Y. Zhang, F. Wang, F. Chu, Y. Yang, H. Li, Z. A Tan, *ChemElectroChem* **2022**, *9*, e202200224.
- [12] C. Bird, A. Kuhn, *Chem. Soc. Rev.* **1981**, *10*, 49–82.
- [13] H. Wang, D. Li, J. Xu, Y. Wu, Y. Cui, L. Chen, *J. Power Sources* **2021**, *492*, 229659.
- [14] a) M. Al Kobaisi, S. V. Bhosale, K. Latham, A. M. Raynor, S. V. Bhosale, *Chem. Rev.* **2016**, *116*, 11685–11796; b) S. V. Bhosale, M. Al Kobaisi, R. W. Jadhav, P. P. Morajkar, L. A. Jones, S. George, *Chem. Soc. Rev.* **2021**, *50*, 9845–9998.
- [15] a) C. Wiberg, M. Busch, L. Evenäs, E. Ahlberg, *Electrochim. Acta* **2021**, *367*, 137480; b) C. Wiberg, F. Owusu, E. Wang, E. Ahlberg, *Energy Technol.* **2019**, *7*, 1900843; c) C. Wiberg, L. Evenäs, M. Busch, E. Ahlberg, *J. Electroanal. Chem.* **2021**, *896*, 115224.
- [16] S. Ahn, J. H. Jang, J. Kang, M. Na, J. Seo, V. Singh, J. M. Joo, H. R. Byon, *ACS Energy Lett.* **2021**, *6*, 3390–3397.
- [17] a) T. Jiao, K. Cai, J. N. Nelson, Y. Jiao, Y. Qiu, G. Wu, J. Zhou, C. Cheng, D. Shen, Y. Feng, *J. Am. Chem. Soc.* **2019**, *141*, 16915–16922; b) L. L. Miller, K. R. Mann, *Acc. Chem. Res.* **1996**, *29*, 417–423; c) I. Tabakovic, L. L. Miller, R. G. Duan, D. C. Tully, D. A. Tomalia, *Chem. Mater.* **1997**, *9*, 736–745.
- [18] a) M.-A. Goulet, M. J. Aziz, *J. Electrochem. Soc.* **2018**, *165*, A1466–A1477; b) F. R. Brushett, M. J. Aziz, K. E. Rodby, *ACS Energy Lett.* **2020**, *5*, 879–884.
- [19] M. Gao, M. Salla, F. Zhang, Y. Zhi, Q. Wang, *J. Power Sources* **2022**, *527*, 231180.

Manuscript received: June 22, 2022

Revised manuscript received: September 13, 2022

Accepted manuscript online: September 19, 2022

Version of record online: October 13, 2022